Proceedings of the ASME 2022 41th International Conference on Ocean, Offshore and Arctic Engineering
OMAE2022
June 5 – June 10, 2022, Hamburg, Germany

OMAE2022-80596

ON ROGUE WAVES GENERATED BY ABRUPT DEPTH TRANSITIONS

Zhenhao Li[1], Tianning Tang[1], Samuel Draycott[2], Yan Li[1,3], Ton van den Bremer[1,4], Thomas Adcock[1]
[1]Department of Engineering Science, University of Oxford
[2]Department of Mechanical, Aerospace and Civil Engineering, University of Manchester
[3]Department of Energy and Process Engineering, Norwegian University of Science and Technology
[4]Faculty of Civil Engineering and Geosciences, Delft University of Technology

ABSTRACT

Wave propagation over variable bathymetry is known as one of the possible mechanisms that can provoke rogue waves. In this paper, we use a fully nonlinear potential-flow solver, OceanWave3D, to simulate the process of waves propagating over variable bathymetry and analyse the kinematics under the free surface near the top of the slope. To achieve this, we first evaluate the accuracy of the numerical results generated by OceanWave3D. We carry out convergence tests to examine the influence of different parameters in OceanWave3D on the numerical results. Based on verification and validation tests, we evaluate the accuracy of OceanWave3D for problems with variable bathymetry comparing numerical and experimental results. We find that OceanWave3D is accurate enough to solve equations for problems with abrupt depth transitions and the agreement between experimental results and numerical results is good. Finally, we investigate the kinematics and we find that a slope can not only amplify crest amplitudes but also increase the wave kinematics near the top of the slope, which has obvious implications for loads on offshore structures.

1 Introduction

Large ocean waves are of interest to scientists and engineers. In particular there is interest in what can cause larger waves than predicted by linear wave dynamics. Various mechanisms have been proposed which might give rise to such so called rogue or freak waves [1–4]. One which has received considerable attention over the past decade is where waves pass over abrupt depth transitions [5–9]. Li et al. [10] argue that the release of bound components as the water depth changes is the primary cause of the excess number of rogue waves which have been observed in experiments and numerically. Modelling these waves passing over abrupt depth transitions to better understand this phenomenon is the subject of this paper.

Ocean waves are typically modelled using potential flow equations. Numerically solving these equations is a well known problem in ocean engineering and a number of techniques exist. Some, such as Green function codes [11] are excellent for solving problems with complex domains but have high computational demands. SPH is also an alternative [12]. Here we examine whether the numerical model OceanWave3D (OW3D) can be used for modelling waves passing over abrupt changes in bathymetry. Following this we exploit the fact that OW3D explicitly solves for the internal kinematics under the waves to do a preliminary investigation of the impact on the fluid motion of the waves passing over the step.

2 Methodology

In this section, the numerical simulation and the experimental set-up are introduced.

2.1 Numerical simulations by OW3D

In this paper, all of the numerical results are generated using OW3D [13]. The code time-marches the classical potential-flow water-wave equations. The code has been extensively used for modelling water wave propagation and kinematic [14, 15]. OW3D is a fully nonlinear potential-flow solver [13]. Potential-flow equations for surface gravity waves are solved by OW3D in a three-dimensional Eulerian frame [13], which gives the kinematics information not only at the free-surface boundary but also at all the vertical nodes hence allowing full kinematic reconstruction. Hence, in this study, the wave kinematics results are extracted directly during the time marching process without any further assumptions. A classical fourth-order Runge-Kutta time marching is applied in OW3D. In OW3D, a σ-coordinate transformation is applied to map the vertical solutions to a time-invariant grid, which can also be used to solve the fully nonlinear potential-flow equations with variable bathymetry. The numerical results from OW3D for nonlinear waves on a semi-circular shoal has been validated against the experiments [16] in previous studies [13].

The numerical domain and wave parameters selected vary depending on the particular case considered. Distances in the horizontal are given by x and in the vertical by z with a datum of mean water level. In the convergence tests presented in §3.1, the length of the numerical domain, L_x, is fixed as 140 times the wave-length (L_x=30,720 m). The time duration of the simulations is equal to 160 times the wave period (t=1920 s). The water depth in the simulation is 500 m (giving non-dimensional depth $kh = 14$). In terms of the wave parameters, the representative wave-length (λ) is 225 m and the wave period (T) is 12 s.

In the convergence test, the values of Δt, Δx and N_z are changed to investigate the influence of different values. The different values of these three parameters and the corresponding number of nodes per wave-length ($\lambda/\Delta x$) or time steps per wave period ($T/\Delta t$) are given in Table 1. The number of nodes on the x-axis, N_x, varies between 2049 and 4097. This results in a variation in Δx between 15 m (15 points per wave-length) to 7.5 m (30 points per wave-length). The value of Δt, the time interval between two time steps, varies between 0.3 s (40 time steps per wave period) and 0.8 s (15 time steps per wave period). The number of nodes in the vertical direction, N_z, is varied between 20 to 40, which are clustered to give greater resolution near the free surface (see equation (4) in [13]).

The numerical domain and wave parameters of the verification and validation tests are presented in Table 2.

In the verification test simulations, the waves are generated and fluxed in from the left boundary of the numerical domain and absorbed on the right. Thus a relaxation zone and a damping zone are used. The relaxation zone is used for generation of the wave in the numerical domain and is located from 0 m to 10 m (3 times the wave-length) on the x-axis. The damping zone, used for wave absorption, is located from 190 m (56.6 times the wave-length) to 200 m (59.6 times the wave-length). The water depth on the deep-water side is 0.55 m (the non-dimensional water depth kh is 1.03) and in shallower-water side is 0.2 m (the non-dimensional water depth kh is 0.37). Therefore, the water depth change (Δh) is fixed as 0.35 m. Although the gradient of the slope changes for different cases from 0.33 to 14, the top of the slope is always located at x=110 m.

Δt ($T/\Delta t$)	Δx ($\lambda/\Delta x$)	N_z
0.30 (40)	7.5 (30)	20
0.34 (35)		
0.40 (30)	12.0 (19)	30
0.48 (25)		
0.60 (20)	15.0 (15)	40
0.80 (15)		

TABLE 1: Different values of Δt, Δx and N_z in OW3D and their corresponding nodes per wave-length ($\lambda/\Delta x$) or time steps per wave period ($T/\Delta t$).

	L_x (m)	N_x	t (s)	Δt (s)
Verification tests	200	32000	120	0.00125
Validation tests	54	3500	64	0.00781

	N_z	kd_s	kd_d	λ (m)
Verification tests	20	0.37	1.03	3.36
Validation tests	20	0.78	1.55	2.23

TABLE 2: Length of the numerical domain L_x, number of nodes on the x-axis N_x, time duration of the simulation t, time interval between two time steps Δt, number of nodes on the z-axis N_z, non-dimensional depth in shallower water kd_s, non-dimensional depth in deeper water kd_d and wave-length λ.

In the validation tests, we use two relaxation zones with 'one iteration' for wave generation, similar to [18]. The first relaxation zone is located from 0 m to 10 m (4.5 times the wave-length) and the second one is located from 10 m (4.5 times the wave-length) to 20 m (9 times the wave-length). The second relaxation zone is implemented mainly to absorb the reflected wave, caused by the reflection of waves reaching the slope. The location of the damping zone is from 44 m (20 times the wave-length) to 54 m (24 times the wave-length). The gradient of the slope is 1, and it is located from 21.5 m to 21.88 m in the numerical domain. However, in the simulation, the wave just leaving the second relaxation zone is not exactly equal to the target initial condition. Therefore, an iterative method is used to reduce the

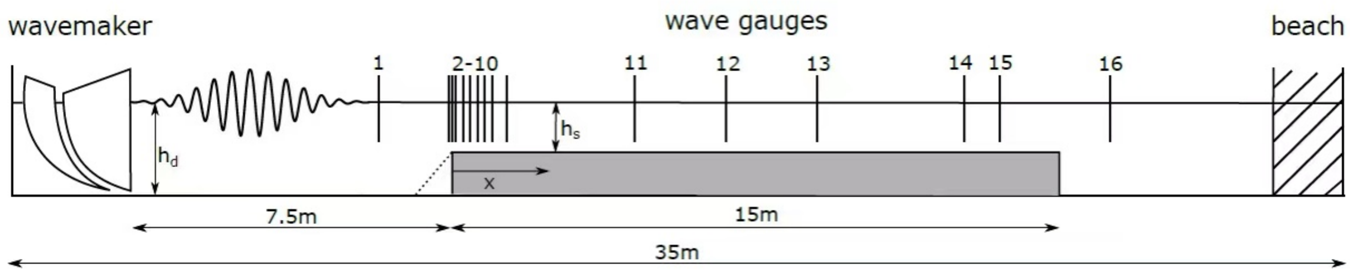

FIGURE 1: Diagram of experimental set-up including gauges, step, beach and wave-maker positions (from [17]).

disagreement between the numerical wave and the initial condition. The iterative method can be performed by finding the difference between the wave just leaving the second relaxation zone and the expected initial condition. Then, we add the difference onto the initial condition and repeat the same simulation again until the wave leaving the relaxation zones agrees with the iterated initial condition.

2.2 Experimental data and set-up

In this paper, all the experimental data are obtained from Li *et al*. [17]. The experimental set-up is presented in Figure 1. A total of 16 gauges were used to measure the waves of which 4 are selected for comparison with the numerical simulations. Data at gauges 1, 3, 8 and 11 are selected, and the location of these is shown in Table 3. The width of the flume is 0.6 m and the length is 35 m. The top of the slope is 7.5 m away from the wave-maker. The water depth of deeper water side, h_d, is 0.55 m and the water depth of shallower water side, h_s, is 0.2 m. Thus the height of the slope is fixed as 0.35 m. The slope is indicated by the dashed line in Figure 1, showing a slope of 1:1.

Gauge no.	1	3	8	11
Position x (m)	-1.88	0.00	0.90	5.00

TABLE 3: The locations of gauges 1, 3, 8 and 11 in the experiment. Position x indicates the distance to the top of the slope, and positive value indicates gauges after the top of the slope (from [17]).

3 Verification

Verification is conducted to make sure OW3D is accurately solving the potential-flow equations for wave propagation over steps. However, we start by considering waves propagating over a flat bed. Whilst the accuracy of OW3D is well established for such a case this is helpful in interpreting our later results when varying bathymetry is introduced.

3.1 Convergence on flat bathymetry

Simulations of unidirectional waves on a flat bathymetry are run first. We do this to understand the impact of numerical discretisation on the accuracy of the solution We use deterministic wavegroups, which we initialise in space using linear theory. The initial wavegroup is given by wave:

$$\eta(x) = Ae^{-\frac{1}{2}S_x^2x^2}\cos(k_p x), \tag{1}$$

where η is the surface elevation, A is the amplitude, S_x is the spatial bandwidth and it is equal to the spectral width for narrow-banded wavegroups and k_p is the peak wavenumber. The group propagates for 160 wave periods and at their steepest the waves would have $Ak = 0.1$ if the evolution were linear. Note that due to non-linear evolution (e.g. [19–21]) the focus amplitude will be slightly higher than the one predicted by the linear theory. In this case, S_x is 0.004606 m^{-1} which a reasonable value for real ocean waves [22].

In Figure 2, the relationship between the error in the numerical results and the value of different parameters in OW3D is presented. We consider three parameters in OW3D: Δt, Δx and N_z, and show the results in subfigures (a,b), (c,d) and (e,f), respectively. In Figure 2, Δt is non-dimensionalised by wave period T and Δx is non-dimensionalised by wave-length λ. The values of Δx, Δt and N_z and their corresponding values of nodes per wave-length ($\lambda/\Delta x$) and time steps per period ($T/\Delta t$) are shown in Table 1. It is worth emphasising the most important information are the number of nodes per wave-length or time steps per wave period rather than the absolute values themselves, which ultimately depends on the value of Δt, Δx and N_z in OW3D. In this simulation, the representative wave-length (λ) is 225 m and wave period (T) is 12 s. If the selected parameters in OW3D are Δx=7.5 m and Δt=0.3 s, it means there are approximately 30

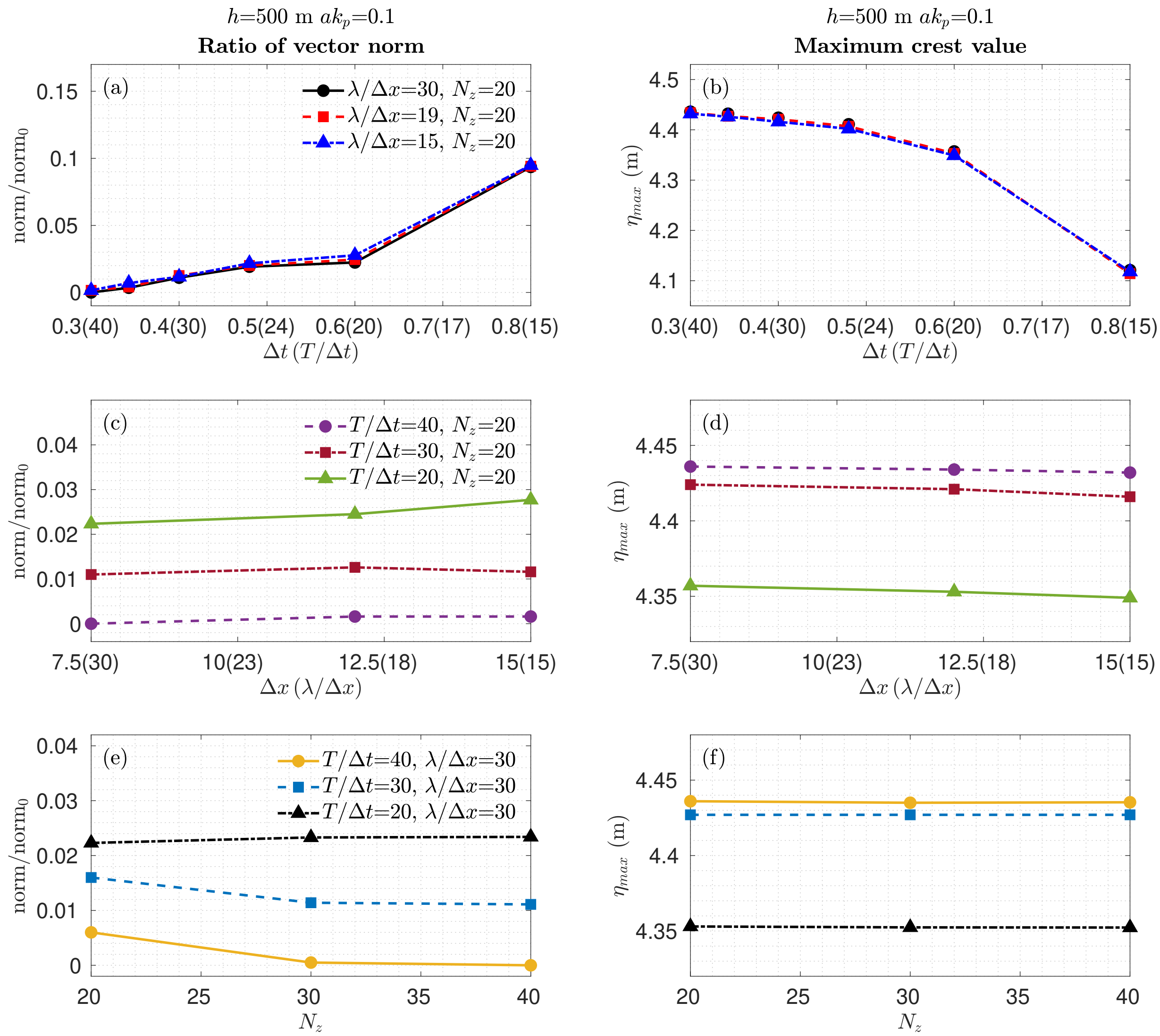

FIGURE 2: Convergence test of different parameters in OW3D for (a,b) Δt, (c,d) Δx, and (e,f) N_z. Parameters are also non-dimensionalised by wave-length (λ) or wave period (T). Δt is the time interval between two time steps. Δx is the spatial interval between two nodes on the x-axis. N_z is the total number of nodes on the z-axis. $T/\Delta t$ is time steps per wave period and $\lambda/\Delta x$ is nodes per wave-length. norm/norm$_0$ is the ratio of vector norm and it is the ratio between the vector norm of difference with the base case and the vector norm of the base case; η_{max} is the maximum surface elevation.

nodes per wave-length and 40 nodes per period, while solving the potential-flow equations in OW3D.

A base case for the convergence tests is defined with $\lambda/\Delta x$=30, $T/\Delta t$=40 and N_z=20. Different values of Δx and Δt are then considered with the variation being presented in Figure 2(a,b), and (c,d). The ratio of the vector norm and the maximum crest values are used to evaluate the difference compared against the base case. The vector norm of the difference is defined by the discrepancy between the wave profile of the base case and the wave profile of one of the other cases ($\|(\eta_0 - \eta)\|$). The ratio of the vector norm (norm/norm$_0$) is defined as the ratio between the vector norm of the difference and the vector norm of the wave profile of the base case ($\|(\eta_0)\|$):

$$\mathrm{norm}/\mathrm{norm}_0 = \frac{\|(\eta_0-\eta)\|}{\|(\eta_0)\|}, \tag{2}$$

in which η_0 is the wave profile for the base case in the simulation and η is the wave profile for the case of interest.

Figure $2(a,b)$ shows how the numerical results change with different number of time steps per wave period ($T/\Delta t$). Firstly, the ratio of the vector norm increases and the maximum crest value decreases when decreasing the value of $T/\Delta t$. This means the difference compared with the base case increases, and the accuracy of simulation decreases. Secondly, below value of $T/\Delta t$ = 20, there is significant variation in the value of ratio of the vector norm and the maximum crest value. Thus, in the simulations used in this paper a maximum timestep of $1/20$ of a wave period is used.

In the convergence test for $\lambda/\Delta x$ and N_z, shown in Figure $2(c,d)$ and (e,f), we can find that there is no significant increase or decrease when changing the value of $\lambda/\Delta x$ or N_z, which means the numerical results are not sensitive to the value of $\lambda/\Delta x$ and N_z for the range of values tested. In each subfigure, there are three lines with different colour and the difference between them is dominated by the different values of $T/\Delta t$. The value of the ratio of between the vector norm and the maximum crest value shows only little change when changing the value of $\lambda/\Delta x$ or N_z. Thus, there are no limitations, within the range tested, with respect to the value of $\lambda/\Delta x$ and N_z when using OW3D.

3.2 Convergence on varying bathymetry

Having examined the propagation of waves on a flat bathymetry in OW3D, we now investigate the accuracy of OW3D when solving potential-flow equations for waves propagating on an abruptly changing bathymetry. To test this, we use the reversibility properties of the governing equations. We run the simulations forward in time up the slope, before reversing the sign of the time step to run the simulations back to the initial conditions. The difference between the initial conditions and the result at the end of the simulations is a rigorous a test of numerical accuracy (see [14, 22]). Similar wavegroups to those in the above test are used. In Figure 3, the relationship between the gradient of slope and the error in the forward/backward simulations is presented.The gradient of the slope is calculated as the ratio between the water depth change or the height of the slope (Δh) and the horizontal span of the slope(Δd):

$$\mathrm{slope} = \frac{\Delta h}{\Delta d}. \tag{3}$$

The water depths are described in §2.1, and the size of the horizontal span of the slope is changed, leading to different value of the slope.

To assess the error in the numerical simulation the vector norm is used ($\mathrm{norm}/\mathrm{norm}_0$). It is calculated as the ratio between the vector norm of the difference between the wavegroup at the start of the forward simulation and the wavegroup at the end of the backward simulation ($\|(\eta_{\mathrm{forward}}-\eta_{\mathrm{backward}})\|$) and the vector norm of the wavegroup at the start of the forward case ($\|(\eta_{\mathrm{forward}})\|$):

$$\mathrm{norm}/\mathrm{norm}_0 = \frac{\|(\eta_{\mathrm{forward}}-\eta_{\mathrm{backward}})\|}{\|(\eta_{\mathrm{forward}})\|}. \tag{4}$$

Therefore, if the value of $\mathrm{norm}/\mathrm{norm}_0$ is smaller, there is less difference between the forward and reverse runs. In Figure $3(a)$, the difference (i.e., $\mathrm{norm}/\mathrm{norm}_0$)) increases as the slope increases. Thus, the simulation error increases for steeper slopes. However, a plateau is reached for slopes steeper than 6, where the ratio converges to a value around 0.05.

In addition, in Figure $3(b,c,d,e)$, we present the comparison between the wavegroup at the start of the forward simulation and the wavegroup at the end of the backward simulation for different slopes. These subfigures show that the agreement between these two wavegroup is visually acceptable for all cases. Thus we have confidence that, at the resolution chosen, OW3D can solve the governing equations accurately even when steep slopes are included in the domain.

4 Validation: comparison with experimental data

We compare numerical and experimental results to understand the difference between actual waves in the experiment and waves generated by the numerical tank.

In the experiment (see §2.2) the wave propagates from deeper to shallow water up a steep slope. The data at probe 1, which is located 1.88 m before the top of the slope, is used as the input to the simulation. The numerical domain and relaxation zones are introduced in Table 2 and §2.1. The numerical bathymetry is the same as the experimental bathymetry and the chosen slope is 1:1. The experimental and the numerical results are compared at gauges 1, 3, 8 and 11. The spatial locations for these 4 gauges are presented in Table 3. After trying different methods to generate the waves in the numerical tank, we find the agreement between the numerical and the experimental results are the best if we use two relaxation zones with one iteration for wave generation. The iterative method is described in §2.1. Thus the comparison at gauge 1 is a test of how accurate we are in initialising our simulations.

In Figure $4(d,e,f)$ show the comparison between the ex-

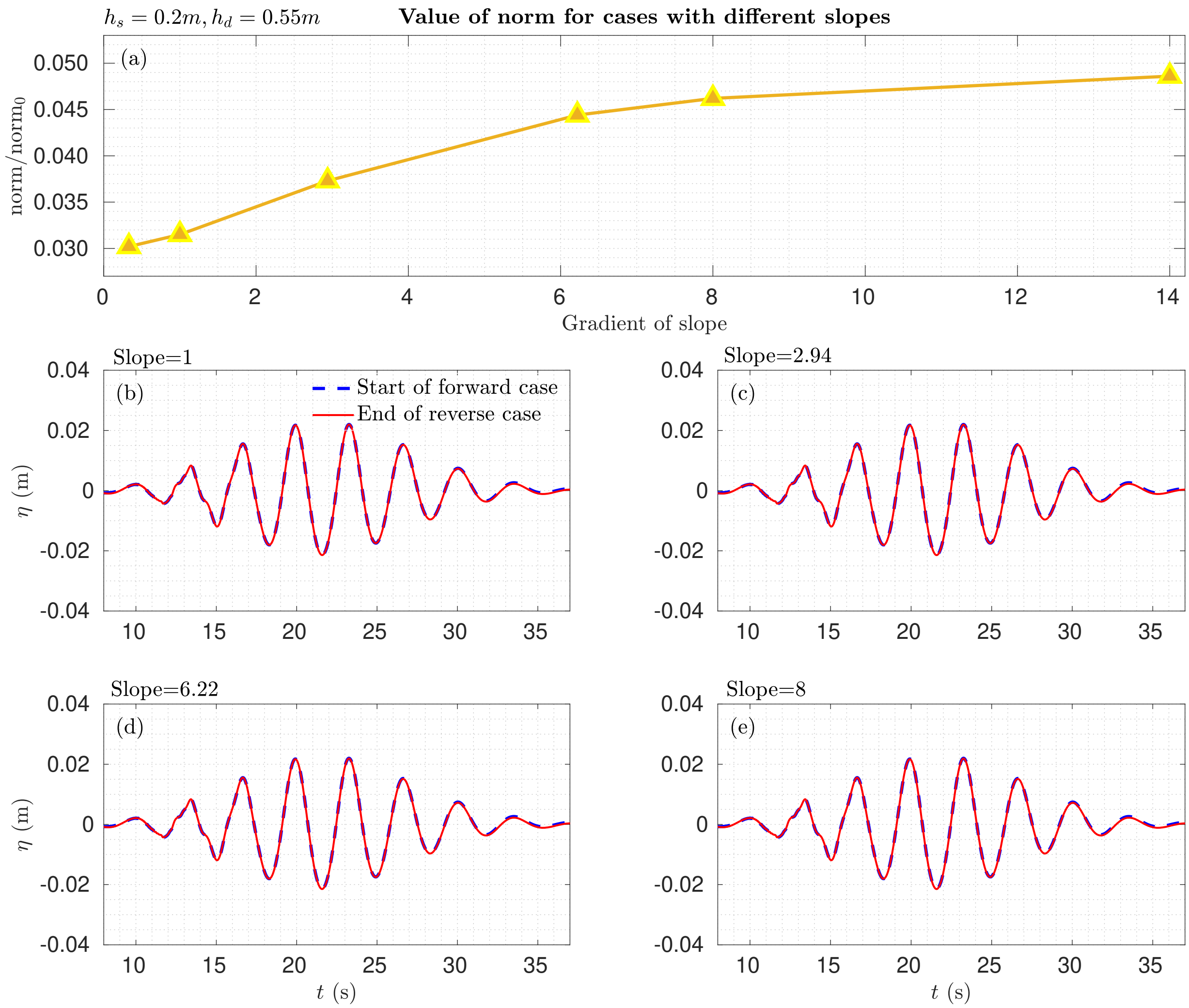

FIGURE 3: Reversibility of OW3D simulation, for (a) the relationship between the gradient of slope and the numerical difference, for (b,c,d,e) the comparison between the wavegroup at the start of the forward case and at the end of the backward case in different slopes. $\mathrm{norm}/\mathrm{norm}_0$ is the ratio between the vector norm of difference and the vector norm of the wavegroup at the start of the forward case; η is the surface elevation and t is time.

perimental and the numerical results at gauge 3, 8 and 11, respectively. We find that the agreement between experiment and simulation is acceptable at all of these three gauges. However, there are small discrepancies, which are further analysed below.

In Figure $4(a,b,c)$, the amplitude spectrum of numerical and experimental results at gauge 3, 8 and 11 respectively are presented. Figure $4(a,b,c)$ show the agreement of the spectrum between experimental and numerical results is good at all three gauges including importantly the higher harmonics after the step.

In order to evaluate the different-order harmonics, frequency filtering is used. In Figure $4(g,h,i)$ and (j,k,l), the first-order harmonics and the second-order harmonics are presented at gauges 3, 8 and 11, respectively. At first and second order, agreement between numerical and experimental results is excellent, and there is no large difference at any gauge. However, for the third order harmonics, shown in Figure $4(m,n,o)$, there are significant discrepancies. The agreement at gauge 8 is good, whereas, at gauge 3 and 11, there is a difference between the experimental

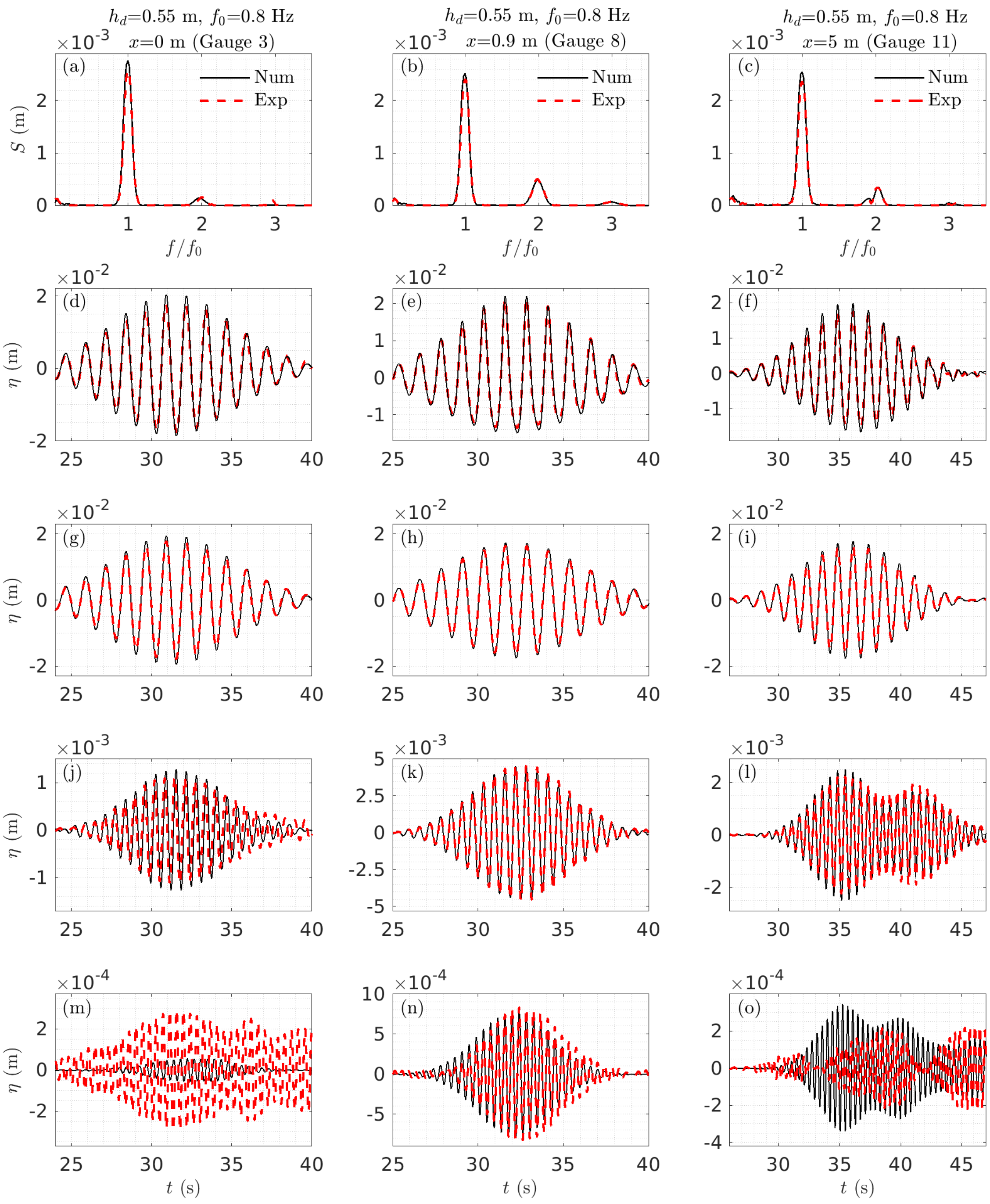

FIGURE 4: Comparison between numerical wavegroups and experimental wavegroups at different gauges. Comparison between the spectrum of numerical and experimental results for (a,b,c), for (d,e,f) the comparison between experimental wavegroup and numerical wavegroup generated using two relaxation zones and one itertaion, for (g,h,i) the first-order harmonics, for (j,k,l) the second-order harmonics and for (m,n,o) the third-order harmonics. η is the surface elevation and f_0 is the peak frequency. t is time, and x indicates the distance to the top of the slope.

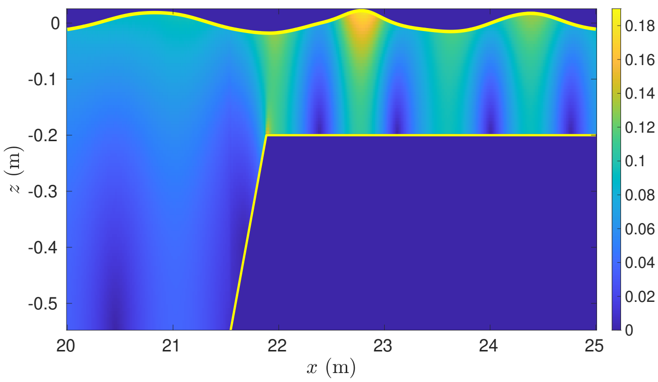

FIGURE 5: Total velocity (m/s) at different horizontal and vertical location at t=31.6 s. x and z represent horizontal and vertical locations. The magnitude of the total velocity corresponds to different colors, shown in colorbar.

and numerical results. One possible reason for this mismatch is the beating effect predicted by Li's theory [23], which are sensitive to small errors in position although this explanation is not fully satisfactory. The amplitude of third order harmonics are relatively small. Thus, the difference is not apparent in Figure 4 (d,e,f).

The results presented here are typical for the other cases considered in [17]. We have not attempted to simulate the 'step' case as we cannot have a perfect step in the OW3D code.

5 Kinematics of wave over variable bathymetry

Having established the accuracy of the code, we now consider how the kinematics of the fluid after the slope. Whilst there is a large literature on waves over slopes, little attention has been paid to the kinematics (they are briefly considered in Lawrence *et al*. [24]) despite the kinematics being critical to loads on structures. Unlike some other numerical schemes (particularly HOS) where kinematics are usually found by post-processing and are not explicitly solved for, OW3D does solve for the water particle movements within the domain. In the present analysis, we continue to investigate the same case as the validation tests and we select a specific region in the numerical domain to study the wave kinematics. We focus on the kinematics from 20 m to 25 m on the horizontal axis and traverses the full depth (z-direction) of the numerical domain.

Figure 5 shows the total velocity at a specific time step (t=31.6 s). We find the velocity increases locally at the top of the slope, and the maximum velocity occurs some distance after the slope. This appears to be consistent with the theory developed by Li [10], where large waves are predicted where the released second-order waves and linear waves come into phase. At the top of the slope itself, there appears to be a localised large velocity near the sea-bed. This is an unsurprising feature of the analysis– one would not expect the classic distribution of wave velocities over the water column at a sharp discontinuity. In fact what is interesting is how localised this is. This helps explain why simplified models which ignore local effects such as [25] show good agreement with numerics and experiments.

We now briefly consider the impact of wave kinematics on loads on offshore wind turbines. Following the recent work of Klahn et al. [26], we use the kinematics to calculate the loads on an offshore structure. Monopiles are common types of offshore structures (e.g., offshore wind turbines), and we can evaluate the wave loading on slender structures based on the kinematics in the absence of the structure [27]. The inertial force is one component of the wave loading and caused by the acceleration of the flow. The inertial force is dominant for cylinder whose diameter is 0.2 times larger than the representative wave-length ($D/\lambda > 0.2$). In this case, a diameter of the cylinder (D) of 0.5 m is selected and the inertial force on the cylinder can be calculated by Morison's equation [28].

$$F(x,t) = \rho \frac{\pi D^2}{4} C_M \frac{\partial u}{\partial t}, \tag{5}$$

where $F(x,t)$ is force per unit length on a fixed vertical cylinder located at a specific spatial location (x), ρ is the water density, C_M is the inertial coefficient ($C_M = 2$) and $\frac{\partial u}{\partial t}$ is the time derivative of the horizontal velocity at corresponding time and space. We note that the Morison calculation is a simplified one– models such as Rainey [29] contain more physics including better modelling the higher order harmonics of the loads [30–32]. We choose to examine the moment on the cylinder around the sea-bed as this is typically the critical load in for structural and geotechnical design of such structures.

After calculating the moment on the cylinder at each time step and each spatial location, we can find the maximum value of the envelope of the moment at each spatial location (from x=21.88 m, the top of the slope, to x=25 m). We run two simulations: one uses the linear version of the code, whereas the other solves the fully non-linear equations. Figure 6 shows the maximum value of the envelope at each spatial location. In Figure 6, the linear case and nonlinear case are compared to investigate the influence of the slope on the higher-order harmonics waves of the wavegroup. We find the maximum value of nonlinear case is larger than that of linear case on the shallower water side. It means the slope not only amplifies the wave crest, but also increases the wave kinematics and the moment on the cylinder. We also see a 'beating' pattern forming (see for instance [33]) which is consistent with the model that amplifications in response are caused by the release of bound waves. Whilst not investigated here, we note that offshore wind turbines are typically designed

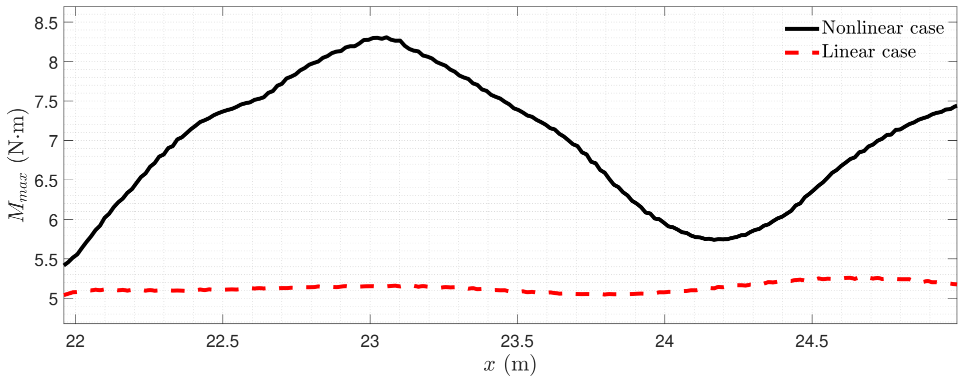

FIGURE 6: Maximum value of the envelope of the moment (M_{max}) at different spatial location (x) for a cylinder whose diameter is 0.5 m. The top of the slope 21.88 m. In the nonlinear case, nonlinear terms of the free-surface boundary conditions are included in the simulation, and in the linear case, numerical waves follow linear wave theory.

so that the resonant frequency is double or treble typical storm waves [34]. Thus loading from released higher harmonics will be particularly important to understand for design.

6 Conclusions

In this paper we have shown OceanWave3D can be used to model waves passing over varying bathymetry including very sharp changes in bathymetry which have attracted considerable interest as a mechanism for generating abnormal waves. We show the code is numerically accurate for modelling such cases. We also show that there is generally very good agreement between numerics and experiments except for the very small third-order components. The accuracy of OceanWave3D appears to be primarily dominated by the timestep at least for the values considered herein.

Although steps have been shown to produce abnormal waves at the top of the slope, these have not so far been linked to loads on structures. Here, we use the kinematics from our numerical simulations to do this. We show that loads on offshore structures are significantly enhanced by the non-linear physics as waves pass over steep slopes, which is of potential concern to offshore engineers.

Future work will look at extending the results in this paper to random waves and to directionally spread waves which are more representative of the waves present in the real ocean.

ACKNOWLEDGMENT

TT and TA are funded by EPSRC grant number EP/V050079/1. TSvB is supported by an RAEng fellowship.

REFERENCES

[1] Dysthe, K., Krogstad, H. E., and Müller, P., 2008. “Oceanic rogue waves”. *Annu. Rev. Fluid Mech.,* ***40***, pp. 287–310.

[2] Adcock, T. A. A., and Taylor, P. H., 2014. “The physics of anomalous (‘rogue’) ocean waves”. *Reports on Progress in Physics,* ***77***(10), p. 105901.

[3] Onorato, M., Residori, S., Bortolozzo, U., Montina, A., and Arecchi, F. T., 2013. “Rogue waves and their generating mechanisms in different physical contexts”. *Physics Reports,* ***528***(2), pp. 47–89.

[4] Kharif, C., and Pelinovsky, E., 2003. “Physical mechanisms of the rogue wave phenomenon”. *European Journal of Mechanics-B/Fluids,* ***22***(6), pp. 603–634.

[5] Trulsen, K., Zeng, H., and Gramstad, O., 2012. “Laboratory evidence of freak waves provoked by non-uniform bathymetry”. *Physics of Fluids,* ***24***(9), p. 097101.

[6] Bolles, C. T., Speer, K., and Moore, M. N. J., 2019. “Anomalous wave statistics induced by abrupt depth change”. *Physical review fluids,* ***4***(1), p. 011801.

[7] Sergeeva, A., Pelinovsky, E., and Talipova, T., 2011. “Nonlinear random wave field in shallow water: variable Korteweg-de Vries framework”. *Natural Hazards and Earth System Sciences,* ***11***(2), pp. 323–330.

[8] Gramstad, O., Zeng, H., Trulsen, K., and Pedersen, G. K., 2013. “Freak waves in weakly nonlinear unidirectional wave trains over a sloping bottom in shallow water”. *Physics of Fluids,* ***25***(12), p. 122103.

[9] Zheng, Y. K., Lin, Z. L., Li, Y., Adcock, T. A. A., Li, Y., and van den Bremer, T. S., 2020. “Fully nonlinear simulations of extreme waves provoked by strong depth transitions: the effect of slope”. *Phys. Rev. Fluids,* ***5***(064804).

[10] Li, Y., Zheng, Y., Lin, Z., Adcock, T. A. A., and van den Bremer, T. S., 2021. “Surface wavepackets subject to an

abrupt depth change. Part 1. Second-order theory". *Journal of Fluid Mechanics,* ***915***.

[11] Xie, C., Choi, Y., Rongère, F., Clément, A. H., Delhommeau, G., and Babarit, A., 2018. "Comparison of existing methods for the calculation of the infinite water depth free-surface Green function for the wave–structure interaction problem". *Applied Ocean Research,* ***81***, pp. 150–163.

[12] Draycott, S., Li, Y., Stansby, P. K., Adcock, T. A. A., and van den Bremer, T. S., 2022. "Harmonic-induced wave breaking due to abrupt depth transitions: An experimental and numerical study". *Coastal Engineering,* ***171***, p. 104041.

[13] Engsig-Karup, A. P., Bingham, H. B., and Lindberg, O., 2009. "An efficient flexible-order model for 3D nonlinear water waves". *Journal of computational physics,* ***228***(6), pp. 2100–2118.

[14] Barratt, D., Bingham, H. B., and Adcock, T. A. A., 2020. "Nonlinear evolution of a steep, focusing wave group in deep water simulated with OceanWave3D". *Journal of Offshore Mechanics and Arctic Engineering,* ***142***(2), p. 021201.

[15] Barratt, D., Bingham, H. B., Taylor, P. H., Van Den Bremer, T. S., and Adcock, T. A. A., 2021. "Rapid spectral evolution of steep surface wave groups with directional spreading". *Journal of Fluid Mechanics,* ***907***.

[16] Whalin, R. W., 1971. *The limit of applicability of linear wave refraction theory in a convergence zone*. Waterways Experiment Station.

[17] Li, Y., Draycott, S., Adcock, T. A. A., and van den Bremer, T. S., 2021. "Surface wavepackets subject to an abrupt depth change. Part 2. Experimental analysis". *Journal of Fluid Mechanics,* ***915***.

[18] Tang, T., and Adcock, T. A. A., 2021. "The influence of finite depth on the evolution of extreme wave statistics in numerical wave tanks". *Coastal Engineering,* ***166***, p. 103870.

[19] Lo, E., and Mei, C. C., 1985. "A numerical study of water-wave modulation based on a higher-order nonlinear Schrödinger equation". *Journal of Fluid Mechanics,* ***150***, pp. 395–416.

[20] Baldock, T. E., Swan, C., and Taylor, P. H., 1996. "A laboratory study of nonlinear surface waves on water". *Philosophical Transactions of the Royal Society of London. Series A: Mathematical, Physical and Engineering Sciences,* ***354***(1707), pp. 649–676.

[21] Adcock, T. A. A., and Taylor, P. H., 2009. "Focusing of unidirectional wave groups on deep water: an approximate nonlinear Schrödinger equation-based model". *Proceedings of the Royal Society A: Mathematical, Physical and Engineering Sciences,* ***465***(2110), pp. 3083–3102.

[22] Gibbs, R. H., and Taylor, P. H., 2005. "Formation of walls of water in 'fully'nonlinear simulations". *Applied Ocean Research,* ***27***(3), pp. 142–157.

[23] Li, Y., Draycott, S., Zheng, Y., Lin, Z., Adcock, T. A. A., and Van Den Bremer, T. S., 2021. "Why rogue waves occur atop abrupt depth transitions". *Journal of Fluid Mechanics,* ***919***.

[24] Lawrence, C., Trulsen, K., and Gramstad, O., 2021. "Statistical properties of wave kinematics in long-crested irregular waves propagating over non-uniform bathymetry". *Physics of Fluids,* ***33***(4), p. 046601.

[25] Massel, S. R., 1983. "Harmonic generation by waves propagating over a submerged step". *Coastal Engineering,* ***7***(4), pp. 357–380.

[26] Klahn, M., Madsen, P. A., and Fuhrman, D. R., 2021. "On the statistical properties of inertia and drag forces in nonlinear multi-directional irregular water waves". *Journal of Fluid Mechanics,* ***916***.

[27] Dean, R. G., and Dalrymple, R. A., 1991. *Water wave mechanics for engineers and scientists*, Vol. 2. World Scientific Publishing Company.

[28] Morison, J. R., , Johnson, J. W., and Schaaf, S. A., 1950. "The force exerted by surface waves on piles". *Journal of Petroleum Technology,* ***2***(05), pp. 149–154.

[29] Rainey, R. C. T., 1989. "A new equation for calculating wave loads on offshore structures". *Journal of Fluid Mechanics,* ***204***, pp. 295–324.

[30] Chau, F. P., and Eatock Taylor, R., 1992. "Second-order wave diffraction by a vertical cylinder". *Journal of Fluid Mechanics,* ***240***, pp. 571–599.

[31] Huseby, M., and Grue, J., 2000. "An experimental investigation of higher-harmonic wave forces on a vertical cylinder". *Journal of fluid Mechanics,* ***414***, pp. 75–103.

[32] Feng, X., Taylor, P. H., Dai, S., Day, A., Willden, R. H. J., and Adcock, T. A. A., 2020. "Experimental investigation of higher harmonic wave loads and moments on a vertical cylinder by a phase-manipulation method". *Coastal Engineering,* ***160***, p. 103747.

[33] Monsalve Gutiérrez, E., 2017. "Experimental study of water waves: nonlinear effects and absorption". PhD thesis, Université Pierre & Marie Curie-Paris 6.

[34] Kallehave, D., Byrne, B. W., LeBlanc Thilsted, C., and Mikkelsen, K. K., 2015. "Optimization of monopiles for offshore wind turbines". *Philosophical Transactions of the Royal Society A: Mathematical, Physical and Engineering Sciences,* ***373***(2035), p. 20140100.